Heterogeneous Catalysis

International Edition: DOI: 10.1002/anie.201914743
German Edition: DOI: 10.1002/ange.201914743

A Robust, Precious-Metal-Free Dye-Sensitized Photoanode for Water Oxidation: A Nanosecond-Long Excited-State Lifetime through a Prussian Blue Analogue

T. Gamze Ulusoy Ghobadi, Amir Ghobadi, Muhammed Buyuktemiz, Elif Akhuseyin Yildiz, Dilara Berna Yildiz, H. Gul Yaglioglu, Yavuz Dede,* Ekmel Ozbay,* and Ferdi Karadas**

Abstract: *Herein, we establish a simple synthetic strategy affording a heterogeneous, precious metal-free, dye-sensitized photoelectrode for water oxidation, which incorporates a Prussian blue (PB) structure for the sensitization of TiO_2 and water oxidation catalysis. Our approach involves the use of a $Fe(CN)_5$ bridging group not only as a cyanide precursor for the formation of a PB-type structure but also as an electron shuttle between an organic chromophore and the catalytic center. The resulting hetero-functional PB-modified TiO_2 electrode demonstrates a low-cost and easy-to-construct photoanode, which exhibits favorable electron transfers with a remarkable excited state lifetime on the order of nanoseconds and an extended light absorption capacity of up to 500 nm. Our approach paves the way for a new family of precious metal-free robust dye-sensitized photoelectrodes for water oxidation, in which a variety of common organic chromophores can be employed in conjunction with CoFe PB structures.*

Introduction

Dye-sensitization is at the heart of several photochemical applications including solar cells, solar energy harvesting devices, and photoelectrochemical cells.[1–3] Recently, this concept has been ingeniously adapted to oxidize water, forming the foundation of dye-sensitized photoelectrosynthesis cells (DS-PECs).[4–9] A DS-PEC architecture consists of a water oxidation catalyst (WOC) coupled to a dye-sensitized metal oxide semiconductor with a large band gap. Two main strategies have been employed so far to improve the rate of the catalytic four-electron water oxidation process and to reduce the back electron transfer in DS-PECs: 1) Connecting the chromophore and the catalyst with appropriate bridging groups forming a dyad[10–12] and 2) introducing secondary electron donor and acceptor groups forming a triad,[13] tetrad,[14] and so on,[15] similar to natural photosynthesis. Recently, numerous molecular-based DS-PECs have been reported.[16–20] While molecular systems offer diversity and high performance, they are limited with precious Ru- and Ir-based WOCs and/or Ru chromophore units. Furthermore, the inherent poor stability (on the order of minutes) of molecular systems has been one of their bottlenecks.[21] Thus, in recent years, finding an earth-abundant alternative for Ru was pointed out as one of the primary perspectives for further implementation of DS-PEC technology.[4,7] Along this path, the use of organic sensitizers has been found to be a promising design strategy for the replacement of Ru-based assemblies.[22] Aromatic macrocycles such as porphyrin and phthalocyanine derivatives have been the most commonly utilized sensitizers among organic based DS-PECs.[23–26] The short excited state lifetime and short hole diffusion length of these dyes, however, generally limit their photocurrent to a value well below 100 $\mu A\,cm^{-2}$, which decays rapidly with a nominal half-life of a couple-to-tens of minutes, limiting their long-term stability for practical usage.[24,25] Moreover, in all of these organic systems, the catalytic site is made of Ir- or Ru-based metalated complexes, which violates the motivation for building an entirely earth-abundant DS-PEC system. In this respect, the use of bulk systems can be considered as a viable approach not only to introduce earth-abundant units to the field but also to improve the stability of such multi-component photoelectrodes. As the only example of an entirely precious metal-free water oxidizing dye-sensitized photoanode, Kirner et al. proposed an organic chromophore sensitized SnO_2 photoanode with a photocurrent, which

[*] T. G. Ulusoy Ghobadi, Prof. F. Karadas
UNAM—National Nanotechnology Research Center, Institute of Materials Science and Nanotechnology, Bilkent University
06800 Ankara (Turkey)
T. G. Ulusoy Ghobadi
Department of Energy Engineering, Faculty of Engineering, Ankara University, 06830 Ankara (Turkey)
A. Ghobadi, Prof. E. Ozbay
Department of Electrical and Electronics Engineering and NANOTAM—Nanotechnology Research Center, Bilkent University
06800 Ankara (Turkey)
M. Buyuktemiz, D. Berna Yildiz, Prof. Y. Dede
Department of Chemistry, Faculty of Science, Gazi University
Teknikokullar, 06500 Ankara (Turkey)
E-mail: dede@gazi.edu.tr
E. A. Yildiz, Prof. H. G. Yaglioglu
Department of Engineering Physics, Faculty of Engineering
Ankara University
06100 Ankara (Turkey)
E-mail: gul.yaglioglu@eng.ankara.edu.tr
Prof. E. Ozbay
Department of Physics, Faculty of Science, Bilkent University
06800 Ankara (Turkey)
Prof. F. Karadas
Department of Chemistry, Faculty of Science, Bilkent University
06800 Ankara (Turkey)
E-mail: karadas@fen.bilkent.edu.tr
Supporting information and the ORCID identification number(s) for the author(s) of this article can be found under: https://doi.org/10.1002/anie.201914743.

decayed from circa 40 to 20 μA cm^{-2} over 5 min.[27] Later, this photoactive chromophore is coupled with a bulk cobalt oxide (CoO_x) WOC layer, in which the catalytic oxide layer also serves as a protective layer for the chromophore during the photoelectrocatalytic process.[28] The system, however, suffered from electron–hole recombination due to the inevitable growth of the CoO_x particles on the semiconductor surface in addition to the organic dye layer and, consequently, resulted in a dramatic decrease in the photocurrent. This deficiency can be mitigated through a molecular dyad strategy in which a covalent linkage will ensure close proximity between the chromophore and WOC and this, in turn, will promote fast and efficient carrier dynamics. It is, therefore, evident that a new chemistry toolbox is necessary for the proper coordination of chromophore and WOC in a three-dimensional bulk system. Beside metal oxide WOCs, cyanide- based extended networks, the so-called Prussian blue (PB) analogues, (PBAs) have also attracted vigorous attention as potential non-oxide heterogeneous WOCs due to their diversity, entirely earth-abundant components, and exceptional stabilities in a wide pH range (from 1 to 13).[29–43] In photoconversion applications, PBAs are essentially used as WOCs for efficient extraction of photogenerated holes of a semiconductor photoanode. We have recently demonstrated that a pentacyanoferrate complex can be used as a bridging group to incorporate an organic chromophore to a PBA structure, thereby forming a robust three-dimensional triad assembly for the light-driven water oxidation process.[29]

Herein, we move a step forward and employ this synthetic methodology to build a robust precious-metal-free dye-sensitized photoanode for water oxidation. The synthesis involves the straightforward coordination of a pentacyanoferrate group to a pyridyl-containing organic chromophore followed by reaction with cobalt ions to build a hetero trifunctional PBA in situ on a rutile TiO_2 nanowire (NW) electrode. The rutile phase has been preferred to anatase since the recombination kinetics for a rutile phase TiO_2 is an order of magnitude slower compared to the latter.[44] Several different pyridyl-containing organic ligands including positively charged nitrogen bearing ones were screened with quantum chemical calculations prior to synthesis. Guided by computational studies, the targeted organic chromophore, in this study, is Janus green B ([JG]), which has a broad absorption response with an upper edge in the near-infrared (NIR) regime. The sensitization ability of JG coordinated PB assembly and the role of each of the components in the electron transfer mechanism and charge separation is discussed based on photoelectrochemical measurements, transient absorption studies, and quantum chemical calculations.

Results and Discussion

Design of the Photoelectrode

Guided by our previous findings, we kept the $[Fe(CN)_5]$ fragment and active Co site unchanged and screened various organic ligands (R) featuring a pyridyl group (Figure 1 a). A combination of up-to-date quantum chemical calculations showed that, in line with our previous results,[29,43,45] the critical LUMO is on the Co−O fragment (Figure 1 a) for the active Co oxo/oxyl species.[48] Moreover, the inclusion of a formal positive charge on the ligand by virtue of quaternized pyridyl salts resulted in a more electrophilic LUMO. This was a hint to exploit ligands, possessing quaternized N atoms, on Fe in order to facilitate the nucleophilic attack of water at the Co−O center. The ground and excited state calculations on the model H_2O−Co−NC−Fe−R systems (Figures S1–7, Tables S1–7) further suggest that LUMO is exclusively located on the chromophore unit. Therefore, the evolution of the presumed active form of the catalyst from H_2O−Co−NC−Fe−R to O−Co−NC−Fe−R can give rise to holes transferring to the catalytically active Co site. Given the aforementioned structural requirements, we further sought commercially available quaternized N dyes with available pyridyl groups. A phenazine-based dye, Janus green B, satisfies these conditions with its available pyridyl nitrogen site and quaternized nitrogen group. Moreover, it exhibits a superior optical response with several absorptions in the visible and NIR regions and possesses several amine groups that can be used to enhance the interaction between the chromophore and TiO_2 surface.

Synthesis and Characterization

An organic-chromophore-coordinated PB structure was obtained with a straightforward two-step synthetic route. First, the amino ligand of $[Fe(CN)_5(NH_3)]^{3-}$ ([Fe–NH_3]) complex was substituted with a pyridyl-containing molecular organic chromophore, [JG] in our case. Then, the [JG]-coordinated pentacyanoiron(II) complex, [Fe–JG], was reacted with Co^{2+} ions to afford a chromophore–PB ([CoFe–JG]) assembly (Supporting Information, Scheme S1). For the preparation of a [CoFe–JG])-modified TiO_2 electrode, an in situ procedure was adapted to maximize the interaction between the semiconductor surface and [CoFe–JG]. Hydrothermally grown rutile TiO_2 NWs on FTO coated glass was soaked in a solution containing [Fe–JG] overnight, forming the dye-sensitized TiO_2 electrode. This resulting electrode is reacted with Co^{2+} ions to obtain PB assembled dye-sensitized TiO_2 working electrode (TiO_2/[CoFe–JG]) (see the chemical structures of photosensitizer-catalyst assembly and the in situ construction on TiO_2 NWs in Figures 1 b,c). The Co sites are coordinated to single/multiple Fe linkers to form an interconnected bulky layer covering the photosensitizer organic molecules. The electrode preparation process is summarized in Scheme S2. A reference electrode was prepared by the sequential dip-coating of a regular CoFe PBA on TiO_2 NWs (TiO_2/[CoFe]). Four dip-coating steps are carried out for PBA layer. The optical images of the bare TiO_2 NWs, TiO_2/[CoFe], and TiO_2/[CoFe–JG]) are displayed in Figure S8 a. Top and cross-sectional SEM images of the TiO_2/[CoFe–JG] photoanode indicate that TiO_2 NWs (with a 1.5 μm length and a circa 100 nm diameter) retain their morphology after [CoFe–JG] coating (Figure 1 d). Transmission electron microscopy-energy dispersive X-ray spectroscopy (TEM-EDS) line scan analysis was performed in the vicinity of the NW

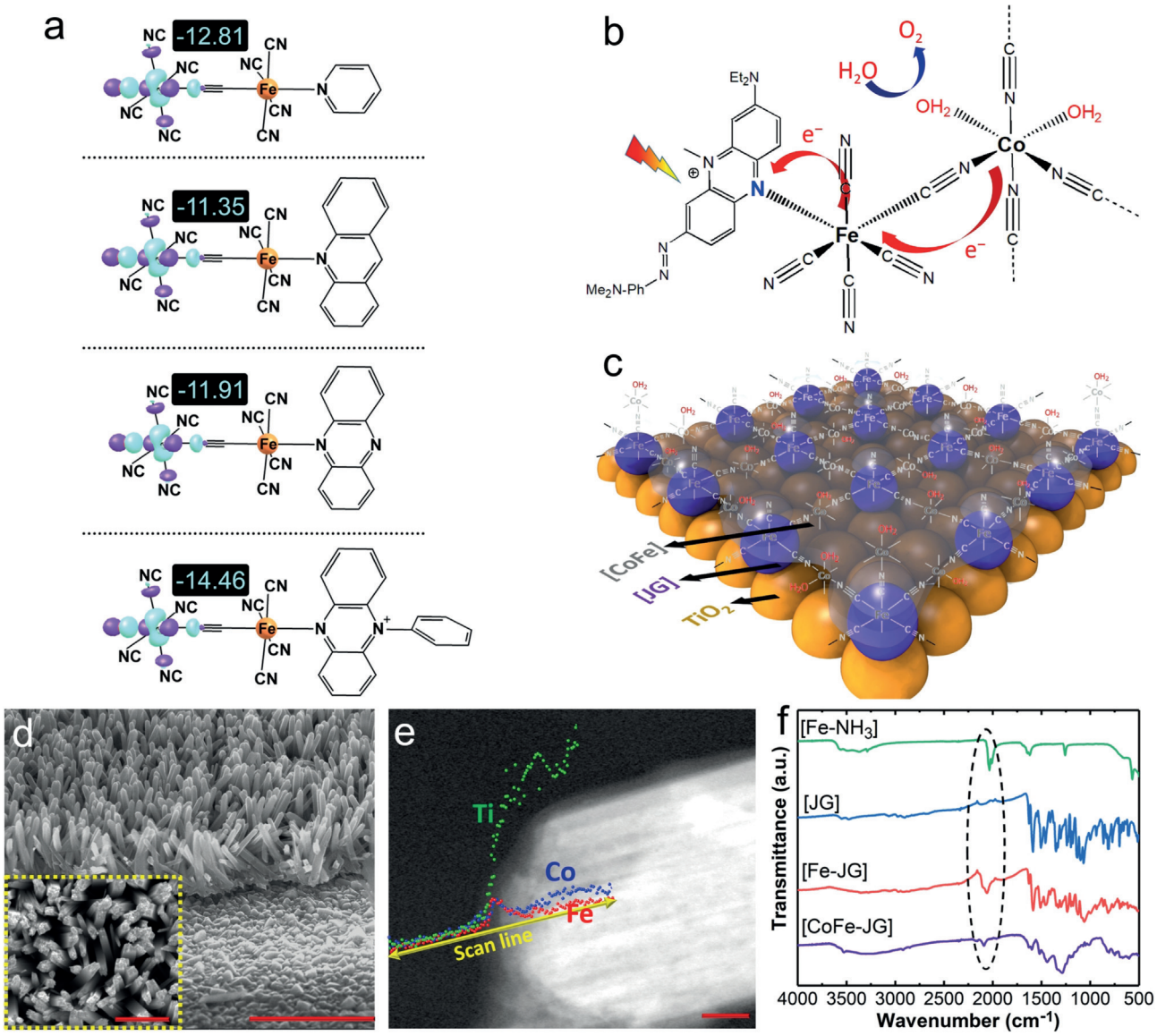

Figure 1. Structural and morphological properties. a) LUMO plots and energies (eV) of the molecules (R) considered for the rational design of DS-PECs. The inclusion of a formal positive charge on the ligand by virtue of quaternized pyridyl salts resulted in a more electrophilic LUMO. b) Chemical structure of [CoFe-JG] assembly. Arrows indicate the electron transfer pathway proceeding from the Co donor to Fe linker and then to JG acceptor group. c) A rough schematic of in situ formation of an ultrathin PB complex on dye-sensitized TiO_2 photoanode yielding TiO_2/[CoFe-JG] electrode. d) A side view of the SEM image of the TiO_2/[CoFe-JG] photoanode, scale bar = 3 µm. The inset shows the top view of the nanowires with the scale bar of 1 µm. e) EDS line scan in HR-TEM from air to an individual PB coated TiO_2 NW with a high magnification of the interface, scale bar = 50 nm. f) ATR-FTIR spectra for [Fe-NH_3], [JG], [Fe–JG], and [CoFe–JG]. The sharp peaks in the 2000–2100 cm^{-1} range are attributed to CN stretch. The peak at around 567 cm^{-1} is attributed to Fe–N coordination bonds. Prominent bands between 1600 and 1330 cm^{-1} are attributed to C=C and C=N stretches of the chromophore structure.

surface to investigate the content of the coating (Figure 1e). The obtained TEM image and TEM-EDS analysis results confirm the formation of an ultrathin [CoFe] assembly with a thickness of around 20 nm on the surface of NW. The infrared spectra (ATR-FTIR) of [JG], [Fe–JG], and [CoFe–JG] exhibit similar features in the 1000–1600 cm^{-1} range confirming the presence of JG in the PB structure. [Fe–NH_3] exhibits a sharp CN peak at 2031 cm^{-1}, which shifts to a higher wavenumber for [Fe–JG] (ca. 2058 cm^{-1}).[29] The blue shift is evidence for not only the coordination of JG to an iron complex but also the donor–acceptor interaction between the iron site and JG, which plays a critical role in efficient electron transfer. The cyanide stretch exhibits a further shift (ca. 2090 cm^{-1}) for [CoFe–JG] due to Fe–CN–Co coordination mode and it is, in essence, a direct evidence for the formation of a PB structure (Figure 1f). A weak signal, observed at 2157 cm^{-1}, indicates the presence of partially oxidized Fe^{3+} and/or Co^{3+} sites. Further analysis of the crystallinity, elemental analysis, morphology of the sensitized NWs, and the infrared spectra of [CoFe–JG] on TiO_2 NWs are provided in Figures S8b–f. The presence of the mixed oxidation states of metal ions in a PB structure is also confirmed by X-ray

photoelectron spectroscopy (XPS) measurements conducted for both the powder ([CoFe–JG]) sample and the photoanode (TiO_2/[CoFe–JG]) (Figures S9–12 and Table S8). The comparison of the N 1s spectra of the precursors and TiO_2/[CoFe–JG] reveals the presence of a cyanide ligand and chromophore units as well as a large number of nitrate anions. The presence of nitrate anions was also monitored by infrared spectroscopy (the peak at 1384 cm^{-1}), which can be attributed to the cationic nature of PB structure as a result of a 3:1 (Co/Fe) stoichiometric ratio obtained by EDX studies.

Photoelectrochemical (PEC) Measurements

The PEC water oxidation measurements were performed with a three-electrode cell using TiO_2, TiO_2/[CoFe], and TiO_2/[CoFe–JG] as working electrodes (see cell configuration in Figure 2a). The linear sweep voltammograms (LSVs) exhibit no significant change in the current density in the absence of light (dark condition) at low overpotentials. At high potentials, above circa 1.6 V vs. RHE, the current density of TiO_2/[CoFe] increases due to the electrocatalytic water oxidation process at the cobalt sites. This feature is, however, less prominent for TiO_2/[CoFe–JG] due to the presence of the insulating JG units, which indicates that TiO_2/[CoFe] serves as a better electrocatalyst than TiO_2/[CoFe–JG]. Interestingly, the trend is quite different under light irradiation condition. Under 1 sun solar light irradiation, without a filter case, the photocurrent performance for TiO_2/[CoFe–JG] is the highest reaching a photocurrent density of 551 $\mu A\,cm^{-2}$ at 1.23 V vs. RHE electrode (Figure S13a). A similar trend was observed with applied bias photon-to-current efficiency (ABPE) plots (Figure S13b). At 0.65 V vs. RHE, TiO_2/[CoFe–JG] electrode shows an ABPE of approximately 0.20%. To have a better qualitative comparison, the photoresponse raised from TiO_2 has been suppressed using a 420 nm cut-off filter. LSV profiles, under visible light illumination, demonstrate a current density of circa 60 $\mu A\,cm^{-2}$ at 1.23 V vs. RHE for TiO_2/[CoFe–JG] electrode (Figure 2b). The bare TiO_2 reveals a photocurrent density of 27 $\mu A\,cm^{-2}$ at the same voltage (originated from the tail absorption of the NW design). The photocurrent response is even poorer for JG sensitized TiO_2 (TiO_2/[JG], without PBA), as explained in detail in the Supporting Information, Figures S14a,b. Since the filter has not completely suppressed the TiO_2 activity, it is essential to scrutinize whether this response arises from the dye absorber layer or from the catalyst-induced enhancement of the TiO_2 host. To answer this question, sequential dip-coating steps were carried out to maximize the PBA loading. As illustrated in Figures S15, the highest light–dark current difference was

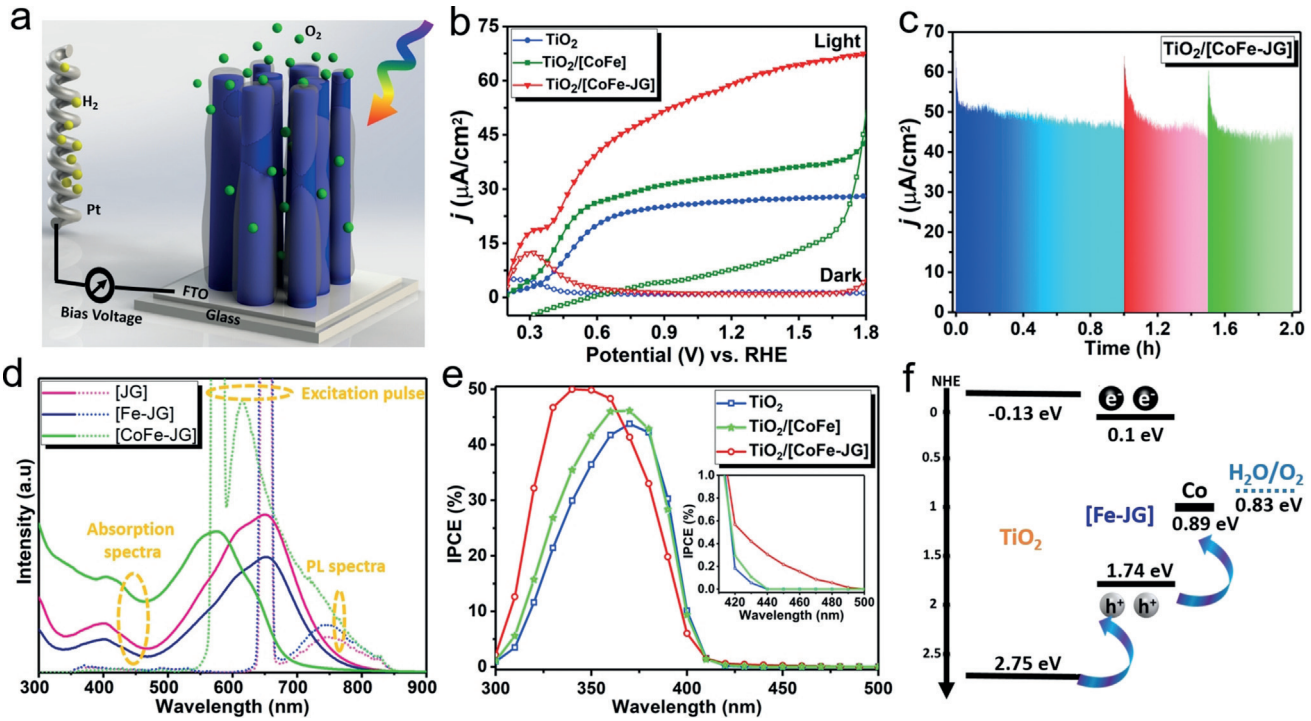

Figure 2. Photoelectrochemical and optical studies. a) Illustrative representations of a 3D schematic of the PEC-WS system consisting of rutile TiO_2 NWs coated FTO electrode loaded with a sensitizer-catalyst dyad, TiO_2/[CoFe–JG] (1.6 cm^2), as a working electrode. b) LSV measurements, *j–V* curves, of the working electrodes under light illumination (solid symbols), under dark (empty symbols) with a white-light source coupled to a 420 nm long-pass filter. Anodic scan rate = 50 $mV\,s^{-1}$, electrolyte: 0.1 M PBS pH 7, light intensity = 100 $mW\,cm^{-2}$. c) Chronoamperogram for 2 h of illumination with a white-light source coupled to a 420 nm long-pass filter at 1.23 V (vs. RHE) bias with a light intensity of 100 $mW\,cm^{-2}$. Different colors indicate the independent measurements of the same TiO_2/[CoFe–JG] electrode at consecutive time slots. d) Absorption spectra of the [JG], [Fe–JG], and [CoFe–JG] solutions. The PL spectra for [JG] and [Fe–JG] solutions with 650 nm excitation wavelength and [CoFe–JG] solution for an excitation wavelength of 575 nm. (10^{-3} M in EtOH solutions, 2 mm cuvette length). e) IPCE spectra of the PECs with a 1.23 V (vs. RHE) external bias. The wavelength was scanned from 300 to 500 nm with a step of 10 nm. f) Schematic energy band diagram of TiO_2/[CoFe–JG] showing the band alignments between different interfaces and the involved water oxidation electron transfer processes.

achieved after four dipping steps. Larger steps do not significantly enhance the photocurrent but rather increase the dark activity. Moreover, TiO_2/[CoFe–JG] electrode exhibits lower dark current densities and a higher onset overpotential compared to those of TiO_2/[CoFe]. Finally, the electrochemically active surface areas (ECSAs) for TiO_2/[CoFe] and TiO_2/[CoFe–JG] have been measured experimentally, as explained in Figures S16 a–c. The ECSA for TiO_2/[CoFe] was found to be higher than that for TiO_2/[CoFe–JG], which can be attributed to the insulating nature of dye molecules that reduces the active sites on TiO_2 surface. These observations suggest that the relative photocurrent enhancement of TiO_2/[CoFe–JG] cannot be explained by an increase in the surface concentration of catalytically active sites. Further evidence on the effect of chromophore to the activity enhancement of the photoanode will be provided in the next sections.

To test the long-term stability of the photoanode, transient photocurrent measurement by the chronoamperometry (CA) technique is conducted on TiO_2/[CoFe–JG] over a total period of 2 h (made of 4 independent time slots) at 1.23 V vs. RHE with regular time intervals while leaving the electrodes in the electrolyte solution. A gradual decrease in the photocurrent density is observed initially, followed by a consistent stable value (around 50 $\mu A\,cm^{-2}$) at each step. (Figure 2 c). This near-constant photocurrent of TiO_2/[CoFe–JG] (unlike TiO_2/[JG] as depicted in Figure S14 a) confirms the stability of the [CoFe–JG] assembly. XPS studies, performed on TiO_2/[CoFe–JG] after long-term CA, also rules out the decomposition of PB structure to metal oxides (Figure S12 b,d). A similar electrolysis experiment at 1.23 V (vs. RHE electrode at pH 7) was performed with a gas-tight cell and the amount of O_2 produced was recorded by GC yielding a Faradaic efficiency of approximately 83 % (as explained in Figure S17), indicating that the photocurrent response is mainly originating from the water oxidation process. Short-term CA for a duration of 300 s in consecutive on–off cycles has also been plotted in Figure S18 a. Moreover, TEM-EDS line scan analysis was performed on TiO_2/[CoFe–JG] after CA measurements, shown in Figure S18 b. The elemental analysis in this figure confirms the existence of the [CoFe] PB structure on the surface of TiO_2 NWs, which confirms the morphological stability of the photoanode. It is noteworthy that the lack of long-term stability is one of the main limiting factors in molecular Ru and organic based dyad systems. Moreover, [JG] belongs to a family of phenazine-based chromophores, which are known to easily decompose under photocatalytic conditions.[46] Therefore, the unprecedented stability of the photoelectrode implies that this methodology can be employed for a variety of organic chromophores even with low photostabilities. The PB network could play a crucial role in the stabilization of the organic chromophore, which is in good agreement with our previous study on a molecular Ru coordinated PBA.[47] LSV measurements under light conditions (with and without filter) were also carried out under an O_2 scavenging electrolyte, which is known as a hole scavenger (h_s), in order to scrutinize the interfacial processes in terms of charge transfer efficiency, η_{CT}. The photocurrent has been significantly improved in a h_s environment (Figures S19 a–c) in the case of 1 sun solar irradiation (unfiltered case). There is, however, a small difference between PBS and h_s electrolyte responses for the LSV results, upon filtering the TiO_2 response. The extracted data shows a near unity η_{CT} maxima (where the dye response is dominant, $\lambda > 420$ nm), while this efficiency is limited to values below 0.8 for unfiltered cases (where the TiO_2 response is dominant) (Figure S19 d). Therefore, from the perspective of interfacial charge transfer dynamics, the TiO_2/[CoFe–JG] electrode exhibits quite efficient charge transfer dynamics.

Steady-State Absorption, Photoluminescence (PL), and Incident Photon-to-Current Conversion Efficiency (IPCE)

[JG] and [Fe–JG] reveal similar absorption trends with a peak at circa 650 nm and a tail extending toward 800 nm, Figure 2 d. The molar extinction coefficients for the dye were found to be in the order of $10^4\,M^{-1}\,cm^{-1}$, as shown in Figure S20. Once the cyanide groups of [Fe–JG] are coordinated to Co^{2+} ions, a blue-shift in the absorption peak (575 nm) is observed. A similar trend is observed for TiO_2-based electrodes. The only difference is the blue shift in peak position (585 nm for TiO_2/[Fe–JG], and circa 540 nm for TiO_2/[CoFe–JG]), which is mainly due to higher refractive index of TiO_2 (compared to ethanol), see Figure S21. The PL spectra of the samples have been explored by an excitation at their main peak wavelength. While the [JG] and [Fe–JG] reveal a weak PL in the circa 700–800 nm range, [CoFe–JG] represents a broad and strong response with a maximum at 615 nm. Therefore, it can be speculated that the PBA assembly tunes the energetic levels of the dye. While these absorption and PL results demonstrate a broad spectral response (covering visible and NIR regimes) and efficient absorption dynamics for [CoFe–JG], the corresponding photocurrent LSV response is rather low, see Figure 2 b. Incident photon-to-current conversion efficiency (IPCE) is measured for all three photoanodes to interpret this unexpected low activity (Figure 2 e). IPCE spectra exhibit a strong UV response for all electrodes. The profiles for bare TiO_2 and TiO_2/[CoFe] samples are similar, with a peak at 370 nm and an edge at 440 nm (the absorption tail of TiO_2). Therefore, the PBA assembly does not tailor the effective optical band gap of TiO_2 and it only facilitates interfacial charge transfer dynamics. However, a broad yet weak visible light response is probed for TiO_2/[CoFe–JG] photoanode. It can be speculated that this weak response is derived from the [JG] chromophore. Nevertheless, this response shows an exponential decline as we go toward longer wavelengths and it becomes near zero at 490 nm. Therefore, a clear mismatch appears between the absorption and IPCE spectra ranges, which requires further exploration. To understand the reason behind the aforementioned discrepancy, the band alignment is extracted for [CoFe–JG] assembly by cyclic voltammetry (CV) measurements (Figure S22 a,b and Table S9). The details of the band alignment extraction are given in the Supporting Information. The optical band gap of TiO_2 NWs is estimated from Tauc plot, as shown in Figure S23. According to the extracted energy diagram, proper alignment is achieved

between the TiO_2 valence band, HOMO of the dye, and water oxidation level. This matching, however, is not realized for the conduction band of TiO_2 and LUMO level of the photosensitizer, see Figure 2 f, which limits the photoconversion efficiencies to wavelengths much smaller than the dye absorption edge. Another reason for the relatively low IPCE could be attributed to ultra-short excited state lifetime of the organic chromophore. This hypothesis is further interrogated by probing ultrafast carrier dynamics using femtosecond transient absorption measurements.

Kinetic Analysis by Femtosecond Transient Absorption (TA) Spectroscopy

TA measurements were performed for [JG], [Fe–JG], and [CoFe–JG] in EtOH to gain an insight into the ultrafast carrier dynamics of the photoanodes, which are explained in detail in the supplementary information section (Figures S24 and S25 and Table S10). In summary, the addition of Co WOC has significantly prolonged the ESA lifetime of [Fe–JG]. Therefore, it can be envisioned that electron injection probability from dye to the TiO_2 could be substantiated in the [CoFe–JG].

To gain insight on carrier dynamics in the ultimate photoanode, dye-loaded TiO_2 NW samples were studied by TA analysis as well. The TA spectra have been collected for all three assemblies upon pumping at 400 nm. The choice of excitation pump wavelength has been justified in the Supporting Information, (Figures S26 and S27). All spectra were fitted by multi-exponential functions and the data is summarized in Table S11. For [JG] and [Fe–JG] on TiO_2 NWs, two main features, ground state bleaching (GSB) and excited state absorption (ESA), are identified clearly, as in the case of ethanolic solutions of [JG] and [Fe–JG] discussed above, see Figures 3 a,b. In addition, a weak stimulated emission (STE) signal at 800 nm was observed with long delay times. Therefore, it can be deduced that excited states undergo ultrafast deactivation into the S_1 edge. CV results reveal that energies of S_1 edge and TiO_2 CB are improperly aligned and, thus, the injection abilities in TiO_2/[JG] and TiO_2/[Fe–JG] are hampered and ultrashort excited state lifetimes are observed. However, for TiO_2/[CoFe–JG], which was probed at several probe wavelengths, neither GSB nor STE signals were observed (see Figure 3 c). TiO_2/[CoFe–JG] exhibits a broadband ESA signal. The decay dynamics of GSB and ESA signals are displayed in Figures 3 d,e. The ESA signals for TiO_2/[JG] and TiO_2/[Fe–JG] decay to zero within the first 10 ps, while it shows a much longer lifetime for TiO_2/[CoFe–JG]. The time evolution of the ESA signal for TiO_2/[CoFe–JG] is probed at three different probe wavelengths; 500 nm, 600 nm, and 700 nm. Two ultrafast decay times of < 100 fs and 2–3 ps are deduced from the fitting parameters. Besides these two fast components, a long lifetime decay (in the order of 200 ps with an amplitude below 10 %), are also present for TiO_2/[CoFe–JG], see Table S11. Moreover, the extracted decay rates for three probe wavelengths (of 500 nm, 600 nm, and 700 nm) are quite similar to each other, Table S11. Lack of the GSB signal, together with the above results, suggests that an efficient injection into TiO_2 NWs occurs in TiO_2/[CoFe–JG]. Equivalently, the assembly of Co catalyst has suppressed the deactivation pathway of the excited states.

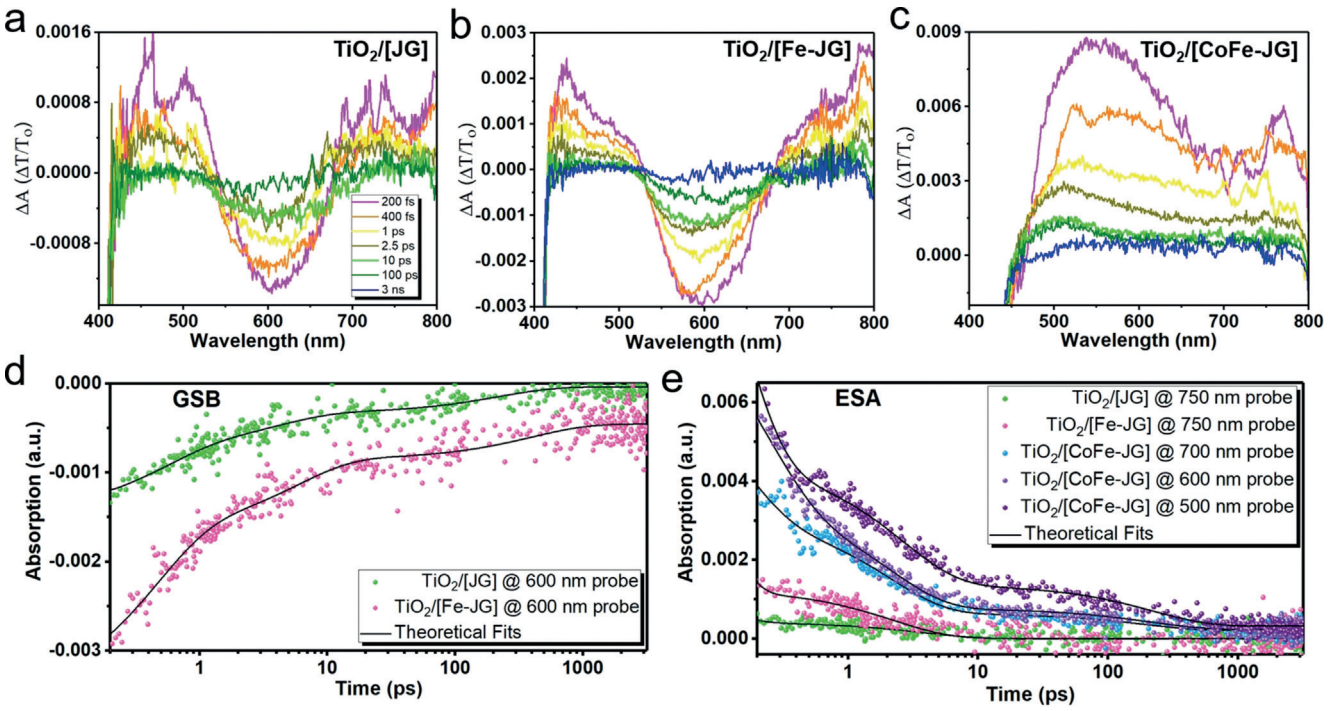

Figure 3. Transient absorption spectra of a) TiO_2/[JG], b) TiO_2/[Fe–JG], and c) TiO_2/[CoFe–JG] compounds at 400 nm (pump) excitation with different pump probe time delays. Decay dynamics for d) GSB and e) ESA signals. The pump pulse intensity for all these measurements is 9.95 GW cm^{-2}.

Further insight into the critical electron transfer events is provided by quantum chemical calculations on the ground and excited states (Figure 4a, Tables S12–16, and Figures S28–36). Although a quantitative treatment of the photoanode is unrealistic, model systems provide valuable qualitative insight into the observed differences of [Fe–JG] and [CoFe–JG] systems as shown in Figure 4a–c. The modulation of the orbital levels upon the inclusion of Co to the system suggests the following: 1) The ligand-centered (LC) $\pi\rightarrow\pi^*$ state is destabilized from 1.27 eV to 3.80 eV. Note also that the character of the excitation changes from phenazine → diazenylaniline to diazenylaniline → phenazine, 2) the lowest metal-to-ligand charge transfer (MLCT) state changes character from Fe → JG to Co → JG, 3) the energy of the lowest MLCT state shifts from 2.61 eV to 1.24 eV, and 4) the Fe-based MLCT state of [Fe–JG] is also destabilized from 2.61 eV to 4.00 eV. Although we should not dwell on the calculated energies in the molecular orbital analysis the qualitative insight brought about is useful and suggests that, upon a mainly LC type of excitation, an electron transfer to the semi-conductor follows. Efficient charge separation is provided by the electron donating ability of Co sites given its properly aligned SOMO state with respect to the doubly occupied orbital on JG. The holes created on JG are transferred rapidly to the SOMO of cobalt, which leads to the activation of the cobalt site for catalytic water oxidation. Thus, the cobalt site emerges as both an electron donor group taking part in electron flow and water oxidation catalytic site. All of these theoretical results are in line with our transient absorption studies and characterizations.

Overall, the addition of cobalt ions changes the optical and electronic properties of the electrode. The lowest transition energy of [Fe–JG] belongs to $\pi\rightarrow\pi^*$ LC state, which cannot inject its electrons to TiO_2 CB due to improper energy alignment.

Furthermore, the excited electrons of [JG] are self-quenched in an ultrafast fashion (within tens of picoseconds) due to the undesirable intermolecular aggregations similar to most of the metal-free organic dyes. Therefore, an ultrafast deactivation of excited electrons into the LC state significantly limits the photoresponse of the phenazine-based dye, see Figure 4b. To increase the excited state lifetime of [JG], the aforementioned deactivation pathway should be eliminated, which is achieved by its conjugation to a PB structure. An in-depth computational and ultrafast transient analysis reveals an unprecedented modification in the electronic and optical properties of [JG] upon its covalent bonding to PB structure. In TiO_2/[CoFe–JG], the energy of the LC state increases (relative to charge transfer states) due to strongly electron donating cobalt sites leading to a prolonged excited state lifetime (in the order of nanoseconds). The electron transfer depicted in Figure 4c also enhances the luminescence yield. The proposed PBA can, thus, be considered as a trifunctional assembly comprised of the following parts: 1) A strong electron donating group, 2) a WOC, and 3) an assembly that modifies the energetic levels of the chromophore (its optical behavior; see Figure 4d).

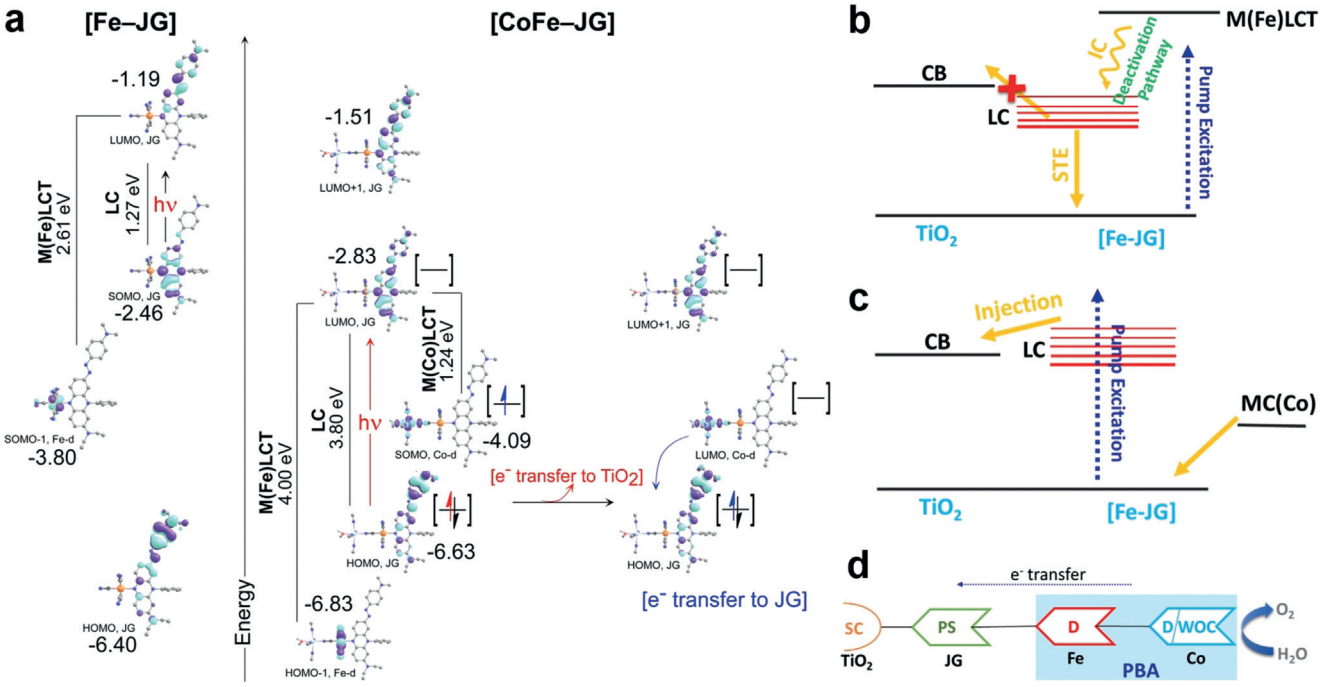

Figure 4. Molecular orbitals and electronic states. a) Critical Kohn–Sham orbitals for [Fe–JG] and [CoFe–JG] systems, (SOMO = singly occupied molecular orbital). Schematic of charge carrier dynamics for b) TiO_2/[JG], TiO_2/[Fe–JG], and c) TiO_2/[CoFe–JG]. d) The summary of electron transfers in TiO_2/[CoFe–JG] (JG: photosensitizer (PS), CoFe PBA: both donor (D) and WOC, and TiO_2: semiconductor (SC). PBA serves as a strong electron donating (D) group, a water oxidation catalyst (WOC), and a tuner for the modification of the energetic levels of the chromophore.

Conclusion

In this work, we demonstrate a strategy and construct, for the first time, an entirely earth-abundant long-term durable dye-sensitized photoanode for water oxidation by utilizing a hetero-multifunctional cyanide-based chromophore–catalyst assembly. While the heterogeneous oxide-based synthetic route yields robust photoelectrodes, the molecular-based approach provides the complete control of the final structure of the photoanode, and hence relatively higher performances. On the other hand, cyanide chemistry offers the engagement of strengths of both of the aforementioned approaches. A computational-study-guided screening was performed to include the key structural elements into the selected chromophore, that is, quaternized nitrogen atom, prior to synthesis. The synthesis involves the coordination of molecular organic chromophore to a pentacyanoiron(II) group, which is completed by reacting with Co^{2+} ions in situ on TiO_2 to obtain a robust heterogeneous photoelectrode. Unlike its superior optical response with an absorption edge in the NIR range, the pristine [JG] chromophore shows poor carrier dynamics with a picosecond excited state lifetime. The conducted TA analysis and quantum chemical calculations demonstrated that excited electrons undergo an ultrafast quenching into the lowest LUMO state with an energetically inadequate position for electron injection. However, the covalent connection of PBA moiety drastically changes the story (Figure 4d). Besides their primary function as catalytic water oxidation sites, the cobalt ions in PB structure serve as donor groups to feed the HOMO level of the dye. Overall, the holes are first transferred to Fe center invoking the $Fe^{2+/3+}$ redox process and then to Co sites to activate them for the catalytic water oxidation process. The efficient charge transfer was achieved also as a result of desirable tuning of the LUMO level of the dye once it is connected to PB structure. Both iron and cobalt sites, hence the PB structure as a whole, serve as the electron-donating group. The short cyanide bridging ligand (with a metal-to-metal distance of circa 5 Å) plays a critical role in the electron donating ability of the catalytic cobalt sites since it provides fast electronic communication between metal ions and the organic chromophore. Thanks to this donation ability, a remarkably long excited state lifetime in the order of nanoseconds is recorded for the photoanode. Moreover, the DS-PEC cell design shows unprecedented stability for a phenazine-type chromophore, which is known to suffer from easy decomposition under photocatalytic conditions. The study marks the first successful attempt to utilizing a phenazine-type chromophore for a dye-sensitized photoanode. The most astonishing conclusion of this study is, thus, the robustness and scalability of the proposed strategy. This work provides an easy-to-employ recipe for the utilization of a variety of pyridyl-containing organic chromophores for various photo-conversion devices including DSSCs and DS-PECs. Therefore, the method proposed herein paves the way for a new family of dye-sensitized photoactive devices that can utilize a variety of organic chromophores even with ultrashort charge separation lifetimes and low photostabilities. Realization of water oxidation photoanodes incorporating a variety of organic dyes with proper electronic band positions (LUMO of dye and conduction band of TiO_2), which utilizes the design principles demonstrated in this work, are under way in our laboratories.

Acknowledgements

This work is supported by the Scientific and Technological Research Council of Turkey (TUBITAK), grant number 215Z249. F.K. and Y.D. thank TÜBA-GEBİP for young investigator awards and BAGEP for young scientist awards.

Conflict of interest

The authors declare no conflict of interest.

Keywords: dye-sensitization · photoelectrochemistry · Prussian blue · water oxidation · water splitting

How to cite: *Angew. Chem. Int. Ed.* **2020**, *59*, 4082–4090
Angew. Chem. **2020**, *132*, 4111–4119

[1] M. Grätzel, *J. Photochem. Photobiol. C* **2003**, *4*, 145–153.
[2] A. Hagfeldt, M. Grätzel, *Chem. Rev.* **1995**, *95*, 49–68.
[3] M. K. Brennaman, R. J. Dillon, L. Alibabaei, M. K. Gish, C. J. Dares, D. L. Ashford, R. L. House, G. J. Meyer, J. M. Papanikolas, T. J. Meyer, *J. Am. Chem. Soc.* **2016**, *138*, 13085–13102.
[4] Z. Yu, F. Li, L. Sun, *Energy Environ. Sci.* **2015**, *8*, 760–775.
[5] F. Li, H. Yang, W. Li, L. Sun, *Joule* **2018**, *2*, 36–60.
[6] D. L. Ashford, M. K. Gish, A. K. Vannucci, M. K. Brennaman, J. L. Templeton, J. M. Papanikolas, T. J. Meyer, *Chem. Rev.* **2015**, *115*, 13006–13049.
[7] R. L. House, N. Y. M. Iha, R. L. Coppo, L. Alibabaei, B. D. Sherman, P. Kang, M. K. Brennaman, P. G. Hoertz, T. J. Meyer, *J. Photochem. Photobiol. C* **2015**, *25*, 32–45.
[8] J. J. Concepcion, R. L. House, J. M. Papanikolas, T. J. Meyer, *Proc. Natl. Acad. Sci. USA* **2012**, *109*, 15560–15564.
[9] P. Xu, N. S. McCool, T. E. Mallouk, *Nano Today* **2017**, *14*, 42–58.
[10] J. R. Swierk, T. E. Mallouk, *Chem. Soc. Rev.* **2013**, *42*, 2357–2387.
[11] S. Berardi, S. Drouet, L. Francàs, C. Gimbert-Suriñach, M. Guttentag, C. Richmond, T. Stoll, A. Llobet, *Chem. Soc. Rev.* **2014**, *43*, 7501–7519.
[12] T. Rawling, C. Austin, F. Buchholz, S. B. Colbran, A. M. McDonagh, *Inorg. Chem.* **2009**, *48*, 3215–3227.
[13] A. Pannwitz, O. S. Wenger, *J. Am. Chem. Soc.* **2017**, *139*, 13308–13311.
[14] L. Favereau, A. Makhal, Y. Pellegrin, E. Blart, J. Petersson, E. Göransson, L. Hammarström, F. Odobel, *J. Am. Chem. Soc.* **2016**, *138*, 3752–3760.
[15] M. Yamamoto, J. Föhlinger, J. Petersson, L. Hammarström, H. Imahori, *Angew. Chem. Int. Ed.* **2017**, *56*, 3329–3333; *Angew. Chem.* **2017**, *129*, 3377–3381.
[16] M. V. Sheridan, B. D. Sherman, R. L. Coppo, D. Wang, S. L. Marquard, K. R. Wee, N. Y. Murakami Iha, T. J. Meyer, *ACS Energy Lett.* **2016**, *1*, 231–236.
[17] L. Alibabaei, R. J. Dillon, C. E. Reilly, M. K. Brennaman, K. Wee, S. L. Marquard, J. M. Papanikolas, T. J. Meyer, *ACS Appl. Mater. Interfaces* **2017**, *9*, 39018–39026.

[18] B. D. Sherman, M. V. Sheridan, K. Wee, S. L. Marquard, D. Wang, L. Alibabaei, D. L. Ashford, T. J. Meyer, *J. Am. Chem. Soc.* **2016**, *138*, 16745 – 16753.
[19] L. Li, L. Duan, Y. Xu, M. Gorlov, A. Hagfeldt, L. Sun, *Chem. Commun.* **2010**, *46*, 7307 – 7309.
[20] H. Li, F. Li, B. Zhang, X. Zhou, F. Yu, L. Sun, *J. Am. Chem. Soc.* **2015**, *137*, 4332 – 4335.
[21] J. W. Youngblood, S. H. A. Lee, Y. Kobayashi, E. A. Hernandez-Pagan, P. G. Hoertz, T. A. Moore, A. L. Moore, D. Gust, T. E. Mallouk, *J. Am. Chem. Soc.* **2009**, *131*, 926 – 927.
[22] D. Wang, M. S. Eberhart, M. V. Sheridan, K. Hu, B. D. Sherman, A. Nayak, Y. Wang, S. L. Marquard, C. J. Dares, T. J. Meyer, *Proc. Natl. Acad. Sci. USA* **2018**, *115*, 8523 – 8528.
[23] J. T. Kirner, R. G. Finke, *J. Mater. Chem. A* **2017**, *5*, 19560 – 19592.
[24] G. F. Moore, J. D. Blakemore, R. L. Milot, J. F. Hull, H. E. Song, L. Cai, C. A. Schmuttenmaer, R. H. Crabtree, G. W. Brudvig, *Energy Environ. Sci.* **2011**, *4*, 2389 – 2392.
[25] M. Yamamoto, L. Wang, F. Li, T. Fukushima, K. Tanaka, L. Sun, H. Imahori, *Chem. Sci.* **2016**, *7*, 1430 – 1439.
[26] M. Yamamoto, Y. Nishizawa, P. Chábera, F. Li, T. Pascher, V. Sundström, L. Sun, H. Imahori, *Chem. Commun.* **2016**, *52*, 13702 – 13705.
[27] J. T. Kirner, J. J. Stracke, B. A. Gregg, R. G. Finke, *ACS Appl. Mater. Interfaces* **2014**, *6*, 13367 – 13377.
[28] J. T. Kirner, R. G. Finke, *ACS Appl. Mater. Interfaces* **2017**, *9*, 27625 – 27637.
[29] T. G. Ulusoy Ghobadi, E. Akhuseyin Yildiz, M. Buyuktemiz, S. Sadigh Akbari, D. Topkaya, Ü. İsci, Y. Dede, H. G. Yaglioglu, F. Karadas, *Angew. Chem. Int. Ed.* **2018**, *57*, 17173 – 17177; *Angew. Chem.* **2018**, *130*, 17419 – 17423.
[30] Y. Aratani, T. Suenobu, K. Ohkubo, Y. Yamada, S. Fukuzumi, *Chem. Commun.* **2017**, *53*, 3473 – 3476.
[31] E. P. Alsaç, E. Ulker, S. V. K. Nune, F. Karadas, *Catal. Lett.* **2018**, *148*, 531 – 538.
[32] Y. Yamada, K. Oyama, T. Suenobu, S. Fukuzumi, *Chem. Commun.* **2017**, *53*, 3418 – 3421.
[33] M. Aksoy, S. V. K. Nune, F. Karadas, *Inorg. Chem.* **2016**, *55*, 4301 – 4307.
[34] M. Szkoda, J. Rysz, J. Ryl, A. Lisowska-Oleksiak, K. Siuzdak, *J. Alloys Compd.* **2017**, *723*, 498 – 504.
[35] K. Trzciński, M. Szkoda, K. Szulc, M. Sawczak, A. Lisowska-Oleksiak, *Electrochim. Acta* **2019**, *295*, 410 – 417.
[36] Y. Yamada, K. Oyama, R. Gates, S. Fukuzumi, *Angew. Chem. Int. Ed.* **2015**, *54*, 5613 – 5617; *Angew. Chem.* **2015**, *127*, 5705 – 5709.
[37] P. Tang, H. Xie, C. Ros, L. Han, M. Biset-Peiró, Y. He, W. Kramer, A. P. Rodríguez, E. Saucedo, J. R. Galán-Mascarós, et al., *Energy Environ. Sci.* **2017**, *10*, 2124 – 2136.
[38] Y. Yamada, M. Yoneda, S. Fukuzumi, *Chem. Eur. J.* **2013**, *19*, 11733 – 11741.
[39] L. Han, P. Tang, Á. Reyes-Carmona, B. Rodríguez-García, M. Torréns, J. R. Morante, J. Arbiol, J. R. Galan-Mascaros, *J. Am. Chem. Soc.* **2016**, *138*, 16037 – 16045.
[40] B. Moss, F. S. Hegner, S. Corby, S. Selim, L. Francàs, N. López, S. Giménez, J. R. Galán-Mascarós, J. R. Durrant, *ACS Energy Lett.* **2019**, *4*, 337 – 342.
[41] F. S. Hegner, D. Cardenas-Morcoso, S. Giménez, N. López, J. R. Galán-Mascarós, *ChemSusChem* **2017**, *10*, 4552 – 4560.
[42] S. Pintado, S. Goberna-Ferrón, E. C. Escudero-Adán, J. R. Galán-Mascarós, *J. Am. Chem. Soc.* **2013**, *135*, 13270 – 13273.
[43] E. P. Alsaç, E. Ülker, S. V. K. Nune, Y. Dede, F. Karadas, *Chem. Eur. J.* **2018**, *24*, 4856 – 4863.
[44] J. R. Swierk, K. P. Regan, J. Jiang, G. W. Brudvig, C. A. Schmuttenmaer, *ACS Energy Lett.* **2016**, *1*, 603 – 606.
[45] E. A. Turhan, S. V. K. Nune, E. Ülker, U. Şahin, Y. Dede, F. Karadas, *Chem. Eur. J.* **2018**, *24*, 10372 – 10382.
[46] T. Ogata, Y. Yamamoto, Y. Wada, K. Murakoshi, M. Kusaba, N. Nakashima, A. Ishida, S. Takamuku, S. Yanagida, *J. Phys. Chem.* **1995**, *99*, 11916 – 11922.
[47] Z. Kap, F. Karadas, *Faraday Discuss.* **2019**, *215*, 115 – 122.
[48] Multi-reference calculations for model systems (Figure S3 and Table S6) also confirmed a local high spin center for the Co–O fragment, in line with our previous reports and as opposed to a recent report by Pires et al. in which a closed shell configuration for the $_{27}Co^{III/IV}$ d^6/d^5 system in a low field ligand environment was proposed. See B. M. Pires, P. L. dos Santos, V. Katic, S. Strohauer, R. Landers, A. L. B. Formiga, J. A. Bonacin, *Dalton Trans.* **2019**, *48*, 4811 – 4822.

Manuscript received: November 18, 2019
Accepted manuscript online: December 14, 2019
Version of record online: February 3, 2020

